Multi-scale characterization of submicronic NASICON-type solid electrolyte Li1.3Al0.3Ti1.7(PO4)3 degraded by spark plasma sintering

Gwenaëlle Courbaron, Rafael Nuernberg, Jon Serrano Sevillano, U-Chan Chung, Mathieu Duttine, Christine Labrugère-Sarroste, Jacob Olchowka, Dany Carlier, Nathalie Delpuech, Laurence Croguennec

Multi-scale characterization of submicronic NASICON-type solid electrolyte $Li_{1.3}Al_{0.3}Ti_{1.7}(PO_4)_3$ degraded by spark plasma sintering

Gwenaëlle Courbaron [a,b], Rafael Bianchini Nuernberg [a *], Jon Serrano Sevillano [a,d,e], U-Chan Chung [a], Mathieu Duttine [a], Christine Labrugère-Sarroste [f], Jacob Olchowka [a,c,d], Dany Carlier [a,c,d], Nathalie Delpuech [b,c,d] and Laurence Croguennec [a,c,d *]

[a] *Univ. Bordeaux, CNRS, Bordeaux INP, ICMCB, UMR 5026, F-33600 Pessac, France*

[b] *Renault SAS, Technocentre, 1 avenue du golf, 78280 Guyancourt, France*

[c] *RS2E, Réseau Français sur le Stockage Electrochimique de l'Energie, FR CNRS 3459, France*

[d] *ALISTORE-ERI European Research Institute, FR CNRS 3104, 80039 Amiens Cedex France*

[e] *CIC Energigune, Albert Einstein 48, Parque Tecnologico de Alava, Miñano 01510, Spain*

[f] *PLACAMAT, UAR 3626, CNRS Université Bordeaux, 33600 Pessac, France*

* corresponding authors: Laurence Croguennec (laurence.croguennec@icmcb.cnrs.fr) and and Rafaël Bianchini-Nuernberg (rafael.bianchini-nuernberg@icmcb.cnrs.fr)

Abstract

One of the most promising and developed disruptive technology of energy storage for the future is all solid-state batteries. The NASICON phase LATP ($Li_{1.3}Al_{0.3}Ti_{1.7}(PO_4)_3$) is widely studied especially thanks to its high ionic conductivity and mechanical strength. However, high temperature densification is required to obtain a dense and conductive material. Here we explore the fast sintering by Spark Plasma Sintering (SPS) of submicronic LATP particles, and the impact of the heating rate on the physico-chemical and transport properties of the pristine powder. High-speed rate for the sintering process induces particles' growth, avoiding any reduction of titanium. The impurity $AlPO_4$ plays a major role on the conductivity, depending on its content but also on its distribution within the composite, either as a coating (surface modification) or as crystalline particles within the grain boundaries. An intimate understanding of the ceramic composites was achieved using combination of advanced characterization techniques to get a multi-scale description of the material, from the pristine to the sintered states, from the surface to the bulk, and from the atomic long range to the local scales. Sharing these fundamental results is essential, with among other motivations, the spreading of our interpretation of complex spectroscopic results (Electronic Spin Resonance (ESR) spectroscopy, solid-state Nuclear Magnetic Resonance (NMR) spectroscopy and X-ray Photoelectron Spectroscopy (XPS)), key for characterization of reactivities at interfaces in this work and in others.

KEYWORDS: NASICON structure, phosphate inorganic electrolyte, Spark plasma sintering, multi-scale reactivity, conductivity, Electronic Spin Resonance spectroscopy, solid-state Nuclear Magnetic Resonance spectroscopy, X-ray Photoelectron Spectroscopy

1. Introduction

Li-ion batteries are widely developed for consumer electronics, mobile phones and more recently for electric vehicles[1]. However, current Li-ion batteries are close to their optimum in terms of gravimetric (300 Wh/kg) and volumetric (800Wh/l) capacities with graphite at the negative electrode and layered oxides of general composition $LiMO_2$ at the positive electrode (mainly $LiNi_{1-x-y}Co_xAl_yO_2$ (NCA) or $LiNi_{1-x-y}Mn_xCo_yO_2$ (NMC))[2,3].That is why already for few years disruptive technologies are studied as Li-sulfur[4], Li-air[5], Redox-flow[6] or all solid-state batteries (ASSB)[7–9]. Although conventional liquid electrolytes demonstrate high conductivity at room temperature (10 $mS.cm^{-1}$), they also suffer from limited stability at high voltage and high temperature[10]. Indeed, due to the presence of flammable and volatile carbonates, leaks and/or explosions may occur. Replacing organic electrolytes by all inorganic solid-state ones could be the key to improve both safety and the energy density. However, a series of challenges remains before introducing full inorganic electrolyte in ASSB such as tailoring the solid-solid interfaces between the solid electrolyte (SE) and the electrodes considering reactivity, transport and mechanical properties.

Among various categories of SEs[11,12], inorganic phosphates having a NASICON-type structure have been one of the most explored. NASICON type materials like $Li_{1+x}M^{III}_xM^{IV}_{2-x}(PO_4)_3$ and especially $Li_{1+x}Al_xTi_{2-x}(PO_4)_3$ (LATP, $0 \leq x \leq 0.5$) attract a lot of interest thanks to their good ionic conductivity (1×10^{-3} S/cm at room temperature[13]), chemical and thermal stability. The NASICON structure of LATP can be described with “lantern” units made of two MO_6 octahedra (with M = Al, Ti) and three PO_4 anionic tetrahedral groups connected by oxygen atoms to form a 3D framework and pathways for Li^+ ions diffusion[14,15]. Partial substitution of Al^{3+} for Ti^{4+} in $LiTi_2(PO_4)_3$ induces an increase of the Li/M ratio for charge compensation (*i.e.* $1Ti^{4+}$ in $LiTi_2(PO_4)_3$ is replaced by ($1Al^{3+}$ + $1Li^+$) in $Li_{1+x}Al_xTi_{2-x}(PO_4)_3$). The lithium ions occupy two different cavities in the LATP structure: the main one called M1 (6b) and the second one M3

(36f) with six and four-fold oxygen coordination respectively. Li^+ migration occurs in LATP hopping through M1- M3 – M3 – M1 sites along zigzag chains as reported in reference[16] which show the lowest activation barrier. The main advantage of Al substitution for Ti is the increase of three orders of magnitude of the ionic conductivity up to 1 x 10^{-3} S/cm for x= 0.3[17,18]. To densify LATP, high temperature sintering is required, typically above 900°C. Different sintering processes are reported in literature. The first one is the conventional sintering process at high temperature (> 900°C). However, the maximum density obtained does not exceed 90%. Indeed, the increase of the sintering temperature leads to an evaporation of Li_2O and formation of cracks caused by anisotropic grain growth[19]. Later, fast techniques were explored, such as Spark Plasma Sintering (SPS)[20], Field Assisted Sintering Technology (FAST)[21], ultra-fast high temperature sintering (UHS)[22] and microwave assisted sintering[23].

In this work, we chose to explore SPS to sinter the NASICON type electrolyte LATP. This technique is a pressure-assisted method in which a direct current is applied to produce heat by Joule effect. The SPS technique allows optimizing sintering time compared to conventional sintering process (from hours to minutes), at lower temperature and with a higher relative density. SPS technique is widely reported in literature to sinter different kinds of materials: Al_2O_3[24,25], $BaTiO_3$[26], ZrO_2[27], etc.[28]… and to assemble different materials according to a one pot process[29]. Since few years, trials have been made to assemble all solid-state batteries by SPS. The first successful results were achieved by Dollé *et al.* [30–32] and since then, as reviewed by Zhu et al.,[33] several research groups work in this direction.

Here, we will demonstrate that the heating rate used during the SPS process has a huge impact on the reactivity, microstructure, crystallinity, and also ionic conductivity, of dense pellets made from a pristine submicronic LATP powder. In-depth insights in the reactivity involved during the sintering process were obtained combining X-ray diffraction to different spectroscopies, the most informative here being Electronic Spin Resonance (ESR) spectroscopy, solid-state Nuclear Magnetic Resonance (NMR) spectroscopy and X-ray Photoelectron Spectroscopy (XPS). Here, even if it was our initial motivation, the goal is not to

report the best sintered LATP ceramic with the optimized conductivity, but to share our multi-scale understanding of the reactivity during sintering and our interpretation of complex results obtained by spectroscopies.

2. Experimental section

2.1 Sample preparation

Submicronic $Li_{1.3}Al_{0.3}Ti_{1.7}(PO_4)_3$ powder was supplied by Marion Technologies (Verniolle, France). Its chemical composition was checked by inductively coupled plasma optical emission spectroscopy (ICP-OES Varian 720 ES), and found to be in good agreement with that expected: Li/Al/Ti/P 1.299 (± 0.005) / 0.310 (± 0.003) / 1.690 (± 0.003) / 3 vs 1.3/0.3/1.7/3 (**Figure S1**). Scanning electron microscopy (SEM) and transmission electron microscopy (TEM) micrographs revealed submicronic primary particles (~100 nm in diameter in average), as shown in **Figure S1**. Before performing sintering, LATP powder was ball milled thanks to SPEX mixer during 30 min inside an agate jar to homogenize aggregates size. To do this, 5 agate beads with a 6 mm diameter were added inside the jar with 5 g of LATP powder. Pellets of 13 mm diameter and 1 to 1.5 mm thickness were prepared by cold pressing applying 370 MPa by means of a manual hydraulic press. Then, for the conventional sintering (CS), these 13 mm pellets were carefully inserted into a tubular furnace at a temperature ranging between 750 and 900°C for 5h or 10h, with heating rate of 3°C/min under air. Other pellets of 10 mm in diameter were densified by SPS, using a SPS 515-S unit Dr Sinter Lab equipped with a 20 V/1500 A generator, a 50 kN press and a 10 mm diameter graphite die. LATP powder is protected from the graphite die using graphite paper (papyex®) at their bottom and top sides, before being inserted in the SPS chamber. An initial working uniaxial load of 3 kN is applied under vacuum (10 Pa). Then, the targeted load of 7.9 kN and the desired temperature are reached applying a high current, which due to the induced Joule effect allows to reach the sintering temperature targeted fast. Our study focuses on the impact of the heating rate on the densification and microstructure modification of the submicronic LATP powder by SPS

process. **Table 1** summarizes all the parameters explored in the frame of this study, considering the load (7.9 kN) and the pellets cross-section area (0.79 cm^2) the applied pressure is of 100 MPa, the sintering temperature of 750°C, the dwelling time of 5 min and the atmosphere is primary vacuum. These parameters have been selected after a large panel of tests playing with different pressures, temperatures and dwelling times, and those were shown to give the best compromise between reactivity and densification, despite differences that will be discussed in the following. The only parameter modified here is the heating rate, ranging from 50°C/min to 300°C/min. The densified pellet obtained by conventional sintering at 800°C during 5h under air was directly compared with all those densified pellets obtained by SPS. The temperature of 800°C during 5h was chosen because these conditions permit to obtain the most densified pellet (90%) by conventional sintering, at a relatively "low" temperature comparable to that used by SPS, and with the smallest amount of secondary phase.

Table 1: Conditions used for SPS sintering and conventional sintering: sintering temperature, pressure, dwelling time, heating rate and relative density given for each sintered sample.

Sample name	Technique	Sintering temperature (°C)	Pressure (Mpa)	Dwelling time (min)	Heating rate (°C/min)	Relative density (%)
LATP 50°C/min	SPS	750	100	5	**50**	95
LATP 73°C/min	SPS	750	100	5	**73**	88
LATP 100°C/min	SPS	750	100	5	**100**	92
LATP 200°C/min	SPS	750	100	5	**200**	95
LATP 300°C/min	SPS	750	100	5	**300**	96
LATP 800°C-5h	Conventional	800	/	300	3	90

2.2 Characterization

Powder X-ray diffraction (XRD) patterns of LATP were recorded before and after sintering on a PANalytical X'pert PRO MPD diffractometer in Bragg-Brentano θ-θ geometry equipped with a secondary monochromator and X'Celerator multi-strip detector. Each routine measurement performed for phase analysis was made within an angular range of 8-80° (2θ), during 34 minutes and using the Cu-$K\alpha_{1,2}$ radiation (λ_1/ λ_2 = 1.54059 Å / 1.54433 Å). For Rietveld refinement and structural characterization, a PANalytical X'pert PRO MPD diffractometer with Bragg-Brentano θ-2θ geometry, equipped for most of them with a front Ge (111) monochromator and a perfectly monochromatic Cu Kα1 radiation ($\lambda = 1.54059$ Å), was used.

Microstructure of LATP was analyzed before and after sintering by high-resolution scanning electron microscope (HR-SEM, Jeol JSM-6700F) after depositing a 1 nm layer of Pt to avoid charging effect.

Electronic spin resonance (ESR) spectra were measured from room temperature down to 30 K with a Bruker ESP300E X-band spectrometer equipped with a liquid helium flow cryostat (Oxford Instruments ESR900). But only the low temperature experiments will be discussed here as Ti^{3+} ESR signals are broadened and almost undetectable at room temperature due to fast spin-lattice relaxation. The ESR experiments were performed using the following parameters: 9.54 GHz microwave frequency, 50 mW microwave power, a magnetic field modulation with 100 kHz frequency and 1 mT amplitude, a spectral resolution of 0.5 mT (sweep width: 500 mT) and a measurement time of 41 ms per point. Analysis of the experimental data was conducted with Bruker *Win-EPR* and *Simfonia* softwares. This technique was used to highlight and quantify Ti^{3+} presence inside LATP after sintering. A set of reference compounds (Ti-doped $KAl_2(SO_4)_2{\cdot}12H_2O$) with known Ti^{3+} concentrations (ranging from 9.1 x 10^{-10} to 9.6 x 10^{-7} mol/g) was also analysed by ESR and then used to estimate the amount of isolated Ti^{3+} ions in the LATP samples.

^{7}Li solid-state Nuclear Magnetic Resonance (NMR) experiments were performed under Magic Angle Spinning conditions (MAS rate 30 kHz) on a Bruker Advance III 100 MHz (2.35 T) spectrometer equipped with a 2.5 mm MAS probe. A rotor-synchronized Hahn echo ($\pi/2 - \pi$)

sequence was used with a $\pi/2$ pulse length of 2.0 µs and a recycle delay of 0.5 s. ^{27}Al and ^{31}P solid-state NMR experiments were performed on a Bruker Advance III 300 MHz (7.05 T) spectrometer equipped with a 2.5 mm MAS probe. ^{27}Al and ^{31}P NMR spectra were recorded with a MAS rate of 30 kHz using a single short pulse ($\pi/12$) sequence (pulse length of 1.12 µs and a recycle delay of 4 s long enough to avoid T_1 saturation effects) and a rotor-synchronized Hahn echo sequence ($\pi/2$ pulse length of 2.0 µs and recycle delay of 10 s), respectively. 1M LiCl, 1M $Al(NO_3)_3$ and 85% H_3PO_4 aqueous solutions were used as external references to calibrate the 0 ppm chemical shift scales. The spectra were fitted using the Dmfit[34] software. These characterizations permit to study the local environment of Li, Al and P in the LATP samples and highlight some differences according to the heating rate used during the SPS process.

Raman spectra were collected with a confocal LabRAM HR Evolution micro-spectrometer from Horiba equipped with a diode 532 nm laser and a 600 gr/mm grating. They were collected in the range of 100-1200 cm^{-1}, using a 10.6 mm focal length lens and with an acquisition time of 15 s and 160 accumulations.

A ThermoFisher Scientific K-ALPHA spectrometer was used for XPS surface analysis with a monochromatized Al-Kα source (hv = 1486.6 eV) and a 400 µm X-Ray spot size. Powders were pressed onto indium foils. The full spectra (0-1350 eV) were obtained with a constant pass energy of 200 eV, while high-resolution spectra were recorded with a constant pass energy of 40 eV. Charge neutralisation was applied during the analysis. High resolution spectra (*i.e.* C 1s, O 1s, Li 1s, Al 2p, Ti 2p and P 2p) were quantified using the Avantage software provided by ThermoFisher Scientific (Scofield Sensitivity Factors).

LATP pellets were sputtered with Au on both sides and set in a two-electrode setup cell to conduct impedance spectroscopy measurements. The impedance spectra were recorded using a Solartron 1260 Impedance/Gain Phase analyzer in the frequency range of 1MHz to 100 mHz, with an applied root-mean-square voltage of 50 mV. Spectra were collected at 25°C at least twice to assure the reproducibility of the measurement. Measurements were performed

from 25 to 85°C to access the dependence of the conductivity on temperature. The impedance data are further analyzed using Zview software (Scribner Associated Inc).

3. Results & Discussion

3.1 Densification of LATP powder by SPS

After spark plasma sintering process, the first impact observed as a function of the heating rate is obviously a change in the colour of the pellets, which are white in their pristine state. Indeed, slow heating rate (50°C/min) induces an intense blue coloration of the pellet, as shown on **Figure 1**. Faster the heating rate (up to 300°C/min), whiter the pellet remains. The colour might be due to the presence of Ti^{3+}, whereas only Ti^{4+} is initially present in LATP. It could be due to a small change in LATP composition which would be compensated by mixed valence of Ti^{4+} and Ti^{3+} within the NASICON structure, or more generally to reactivity during sintering that leads to modification or degradation of LATP. Noh *et al.*[35] studied the densification of nanocrystalline TiO_2 by SPS and proposed the reduction of titanium during the SPS process due to a contact of the powder with the carbon mould and possible formation of gases such as CO. Fast heating rate allows limiting side reactions such as reduction, because overall electric current effects are limited[36].The electron scattering can cause defects such as dislocations, voids or impurities and creation of hot spots which enhance the lattice vibration energy. However, this phenomenon in the case of LATP can, by heat, reduce the Ti^{4+} into Ti^{3+} because of the faster defect motion in SPS. Indeed, densification mechanisms depend on the powder particle size as well as sintering temperature and pressure applied, and these mechanisms can be altered by the electric current applied[37]. By increasing the heating rate, the current applied is increased, the mechanisms involved could thus be affected. In order to test the reduction hypothesis, the blue sample recovered after a SPS sintering applying a heating rate of 50°C/min was re-oxidized using a thermal treatment at 700°C during 12h under O_2. After this heat treatment, the opaque white colour characteristic of LATP sintered samples was recovered.

Change in the density as a function of the sintering heating rate is given in **Figure 1b** with an error ≤ 2 % between pellets sintered with the same parameters by SPS. The results show that 95% of relative density can be reached, either at slow heating rate (50°C/min) but with a significant reduction of the powder, or at faster heating rate (200°C/min) with a mitigated reduction in that case. These latter conditions appear thus as an optimum, a trade-off between titanium reduction and densification at 750°C.

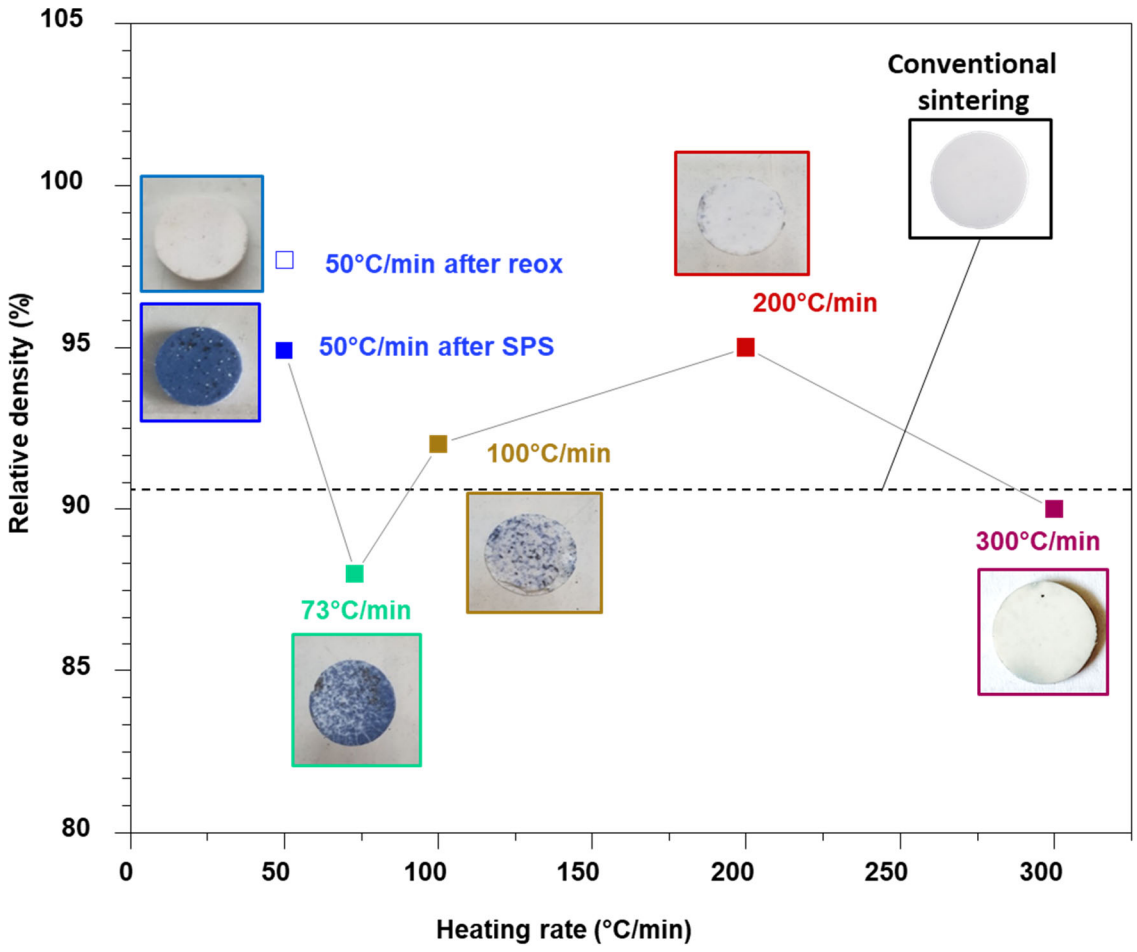

Figure 1: Changes in the relative density and colour of LATP pellets sintered at 750°C during 5 min using different heating rates. The relative density obtained by conventional sintering is given by the horizontal dashed line.

An XRD pattern was collected for each sample: pristine LATP powder, densified pellets at different heating rates ranging from 50°C/min to 300°C/min, the re-oxidized sample at 700°C and, for comparison, the conventional sintered sample at 800°C, during 5h. The patterns

obtained for the series of densified pellets are very similar to that of the pristine LATP powder given as reference in

Figure 2 in the limited angular range 10° to 40° (2θ) in **Figure 2b**, the extended range being available in **Figure 2a.** These patterns exhibit mainly diffraction peaks typical of the LATP NASICON structure described in the *R-3c* space group (JCPDS N°35-0754). Nevertheless, the commercial submicronic LATP powder contains small amounts of impurities. The first, $Li_4P_2O_7$, can be identified, thanks to an enlargement (by 20) (

Figure 2**b)**, by the presence of diffraction peaks localized at 22.5°, 26.9°, 27.7°, 28.2°and 34.6° (2θ) and the second, $AlPO_4$, by diffraction peaks at 21.6° and 23.2° (2θ). After sintering, the impurity $Li_4P_2O_7$ cannot be observed anymore by XRD, independent of the heating rate. On the contrary, the impurity $AlPO_4$ remains but its content seems to decrease with faster heating rates. These results suggest a reactivity between the different components of the pristine powder (LATP, $Li_4P_2O_7$ and $AlPO_4$) during the sintering made by SPS, and thus a homogenization of the material. For the conventional sintered sample, the intensity of the diffraction lines associated to $AlPO_4$ impurity is higher than for the samples sintered by SPS, suggesting a higher content. In addition to $AlPO_4$, rutile TiO_2 is also identified at 20.5° (2θ). Note that the identification of impurities is difficult in these compounds, because they are mainly present in small quantities and different natures depending on sintering conditions. Moreover, it appears that the faster the heating rate, the narrower the diffraction peaks are: the full width at half maximum of the (113) line ($FWHM_{(113)}$) decreases from ~ 0.1523° for the pristine powder to ~0.0396° for the sample SPS 200°C/min. The combination of all these observations reveals thus that the crystallinity and the homogeneity of the material increase during sintering, with an increase of the crystalline domain size from 50 nm for the pristine LATP to more than 300 nm for the sample SPS 200°C/min. At lower heating rate (50°C/min), the crystalline domain size is of 80 nm after sintering by SPS, and of 100 nm after the re-oxidation treatment. For comparison, $FWHM_{(113)}$ is ~ 0.1304° for the sample sintered by the conventional method with crystalline domain size of 100 nm. Therefore, the SPS method can,

rather counter-intuitively at high heating rates, lead to a significant impact on the powder crystallinity whereas it is not the case for conventional sintering.

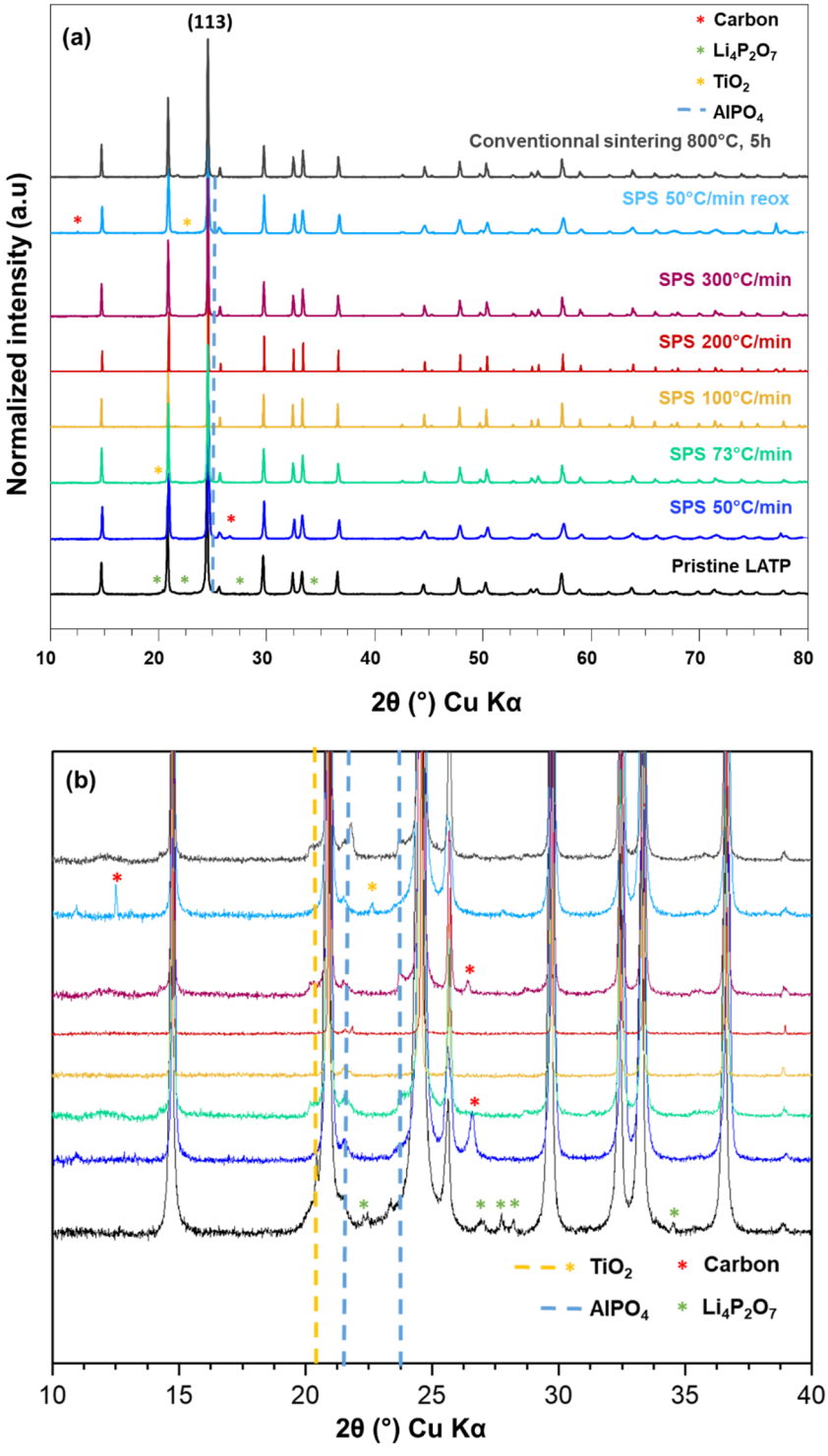

Figure 2: XRD patterns of the pristine LATP powder, the samples sintered by SPS using heating rates ranging from 50°C/min to 300°C/min, the re-oxidized sample and the conventional sintered sample (a).

A zoom of the background was done in order to highlight the presence of impurities, some of them (not marked) being not identified (b).

Rietveld refinements of XRD patterns collected for the pristine LATP powder and the samples sintered by SPS using heating rates from 50°C/min to 200°C/min are given in **Figure S2**. They reveal a good minimization of the difference between the experimental and the calculated patterns, and a significant variation of the lattice parameters and cell volumes among the samples depending on their sintering "history". The refinements were done without considering the presence of impurities, as in small amount and, in addition, non-identified for some of them. The cell parameters as determined are compared in **Table S1**. Two main observations can be done (**Figure S3a**). When the LATP powder is sintered at 750°C with a slower heating rate (50°C/min), the cell parameters vary from 8.505(2) Å to 8.481(3) Å and from 20.845(5) Å to 20.884(9) Å for *a* and *c*, respectively. These variations lead to a cell volume shrinkage from 1305.8(6) $Å^3$ to 1300(1) $Å^3$, which is in apparent disagreement with titanium reduction from Ti^{4+} to Ti^{3+} as their ionic radii in octahedral coordination are of 0.605 Å and 0.67 Å, respectively[38]. This would thus suggest a variation in the LATP composition which is in good agreement with the phase analysis just discussed. For instance, the incorporation of Al to the LATP structure should decrease the cell parameters since the ionic radius of Al^{3+} is about 0.535 Å in octahedral coordination. When the heating rate gets faster (from 73°C/min to 300°C/min), a steady state seems to be reached as the lattice parameters *a* and *c* remain rather constant. All these sintered NASICON-type materials are characterized by cell parameters smaller than those of the NASICON phase in the pristine powder, revealing an enrichment of the composition in Al. The comparison with the lattice parameters reported in **Figure S3b** for $Li_{1+x}Al_xTi_{2-x}(PO_4)_3$ with x varying from 0 to 0.5[39] suggests a composition close to x = 0.1 for the NASICON LATP phase contained in the pristine powder and close to x = 0.3 - 0.35 for the powder sintered by SPS at the faster heating rates (73°C/min and more) and for the powder sintered conventionally, i.e. a composition $Li_{1.3}Al_{0.3}Ti_{1.7}(PO_4)_3$ for the NASICON phase[39]. All these observations show that

a homogenisation of the powder occurs during the sintering process, with the disappearance of the impurity $AlPO_4$ due to its reactivity with the pristine LATP phase and an enrichment of the NASICON phase in Al.

HR-SEM was performed to observe differences in morphology and grain size between the pristine powder and the samples sintered either by SPS or by conventional process. As shown in **Figure 3a**, the primary particles observed in the pristine LATP powder are around 50 - 150 nm in diameter and they are agglomerated in aggregates larger than 10 μm. Once heated in the SPS chamber at 750°C during 5 min, the LATP powder is sintered partially for a slower heating rate of 50°C/min, and more and more for faster heating rates (**Figure 3b-e**). For the sample SPS 50°C/min, the primary particles are still observed within the densified aggregates. At faster heating rates, the fraction of individual primary particles decreases and the grain boundaries disappear, which leads to an increase of the density up to 95 % for the sample SPS 200°C/min. Note that these observations are in good agreement with the increase of the cristalline domain size observed by XRD at heating rates of 73°C/min and above. **Figure 3c-e** show that by SPS, even with a limited time spent at 750°C, the LATP particles are well sintered together, whereas in literature the range of temperatures required to sinter LATP by conventional method is 800°C - 1100°C, and in some cases even by fast sintering[40,41]. No further densification could be achieved by SPS at a higher temperature, of 900°C for instance. Pores can be distinguished for the sintered samples SPS 100°C/min, SPS 200°C/min and SPS 300°C/min. They are likely to be thermodynamically stable pores stemming from the sintering process and in some cases they might never vanish from the sample. This explains why it is difficult to get fully densified ceramic materials. For comparison, SEM images of the conventionally sintered sample were also recorded (**Figure 3f**). In this case, even more pores seem to be present, which is consistent with the lower density obtained of 90% for this sample. Moreover, the primary particle size seems to be bigger than 1 μm with most of the grain boundaries having also disappeared. A grain growth is thus also observed for the conventional sintering as it was identified by XRD[42].

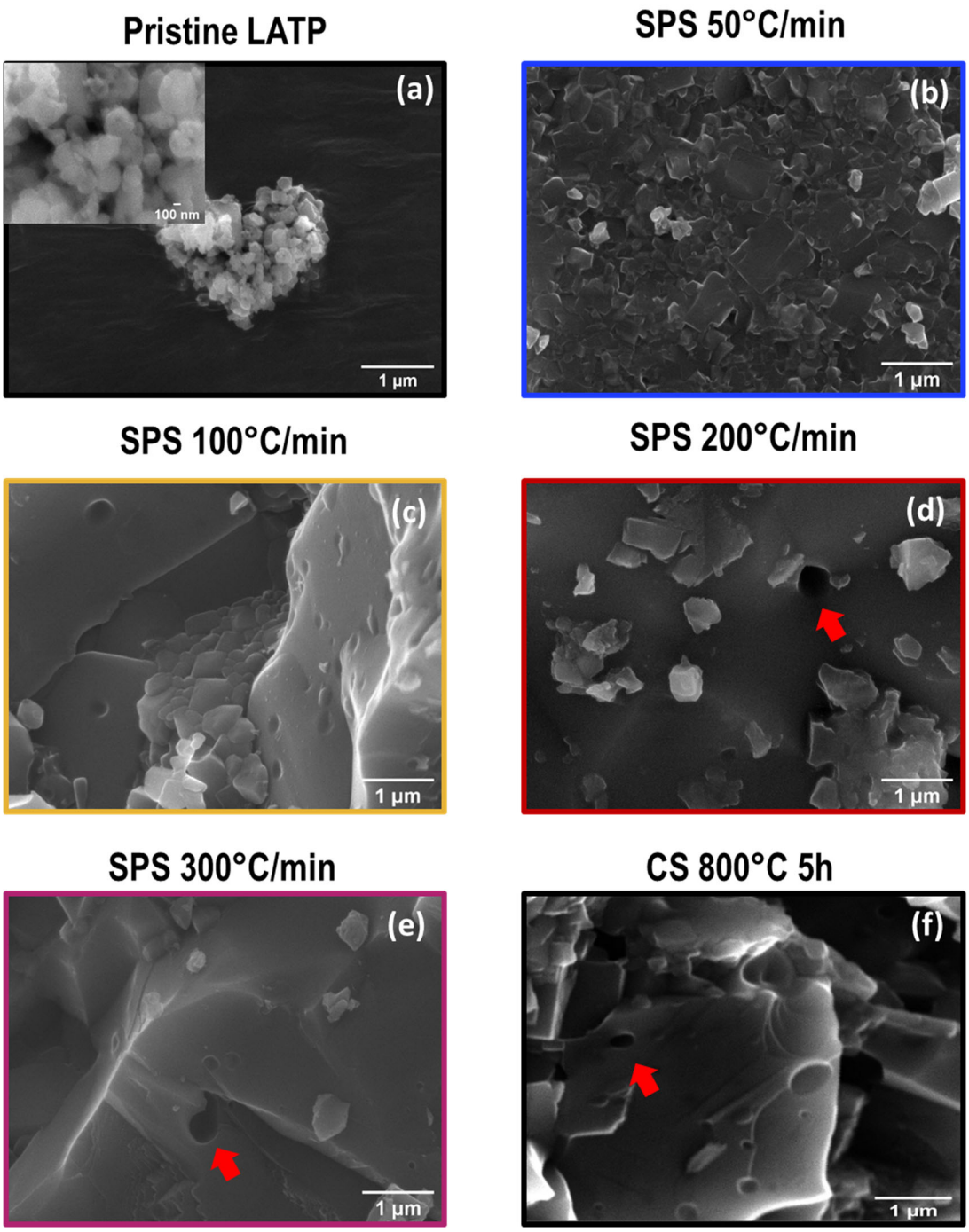

Figure 3: Secondary Electron HR-SEM images of pristine LATP powder (a), samples sintered by SPS at 750°C during 5 min and using heating rates of 50°C/min (b), 100°C/min (c), 200°C/min (d) and 300°C/min (e), and the conventional sintering sample (f). The red arrows identify clear holes in densified powders and suggest possible gas loss during sintering.

As a summary of this first part, we have shown that sintering of 50-150 nm submicronic LATP particles is possible by SPS and 95 % of densification can be achieved compared to 90 % by conventional sintering. Nevertheless, the sintering conditions have to be carefully chosen in

order to balance the densification versus the mitigation of the reactivity. That latter is directly visible thanks to the bluish coloration of the pellets initially white. On the contrary to conventional sintering, SPS allows simultaneously increasing crystallinity and densification of LATP powder in few minutes and at a temperature as low as 750°C.

3.2 Reactivity occurring during LATP sintering by SPS

Electronic spin resonance (ESR) experiments were conducted at low temperature (30 K) in order to determine if the blue coloration of LATP pellets observed by SPS performed at "slow" heating rates is related to the partial reduction of diamagnetic Ti^{4+} to paramagnetic Ti^{3+} ($3d^1$). As expected, no ESR signal was detected for the pristine LATP compound (**Figure 4**) which supports the absence of any Ti^{3+} within the structure prior to any sintering treatment. On the contrary, the sintered sample SPS 50°C/min, which is dark blue, exhibits a sharp and intense axial signal characterized by $g_{//} = 1.960$ and $g_{\perp} = 1.822$. Actually, a careful examination of the line shape of the ESR spectrum along with simulation shows the presence of an additional signal with different *g*-factor values, *ie* $g_{//} = 1.86$ and $g_{\perp} = 1.91$ (**Figure S4**). These two signals, which are labelled Ti^{3+}(A) and Ti^{3+}(B), respectively, can be associated with isolated Ti^{3+} centres with different local symmetry involving oxygen vacancies and tetragonal distortion of the coordination polyhedron (compression when $g_{\perp} < g_{//}$ and elongation when $g_{\perp} > g_{//}$)[43–46]. Finally, a broad resonance line (peak-to-peak width: 28 mT) is also detected at lower fields ($g_{obs.} = 2.3$) and may be due to some exchange-coupled Ti^{3+} clusters. After re-oxidation treatment (700°C during 12 hours under O_2), all ESR signals disappeared (**Figure 4**) as the sample colour changed from blue to white. This confirms the previous attribution of the observed ESR signals to Ti^{3+} species (isolated centres and clusters) which are clearly related to the blue coloration of the SPS (50°C/min) sintered sample. The faster the heating rate used by SPS, the whiter the pellets remain and the less intense the isolated Ti^{3+} ESR signals are. Indeed, the content of isolated Ti^{3+} was estimated to be about 2.2 mol.% for the SPS 50°C/min sample and about 0.8 mol.% for the SPS 73°C/min sample. For the samples sintered with faster SPS heating

rates, the observed broad and unresolved ESR signals ($g_{obs.} > 2$) could be due to the formation of large Ti^{3+} clusters within the LATP structure or Ti^{3+}-rich secondary phases, both involving strong ferro- or antiferromagnetic interactions. Finally, ESR experiments clearly show that slow SPS heating rates promote the formation of isolated Ti^{3+} centres, responsible for the dark blue coloration of the sintered LATP samples.

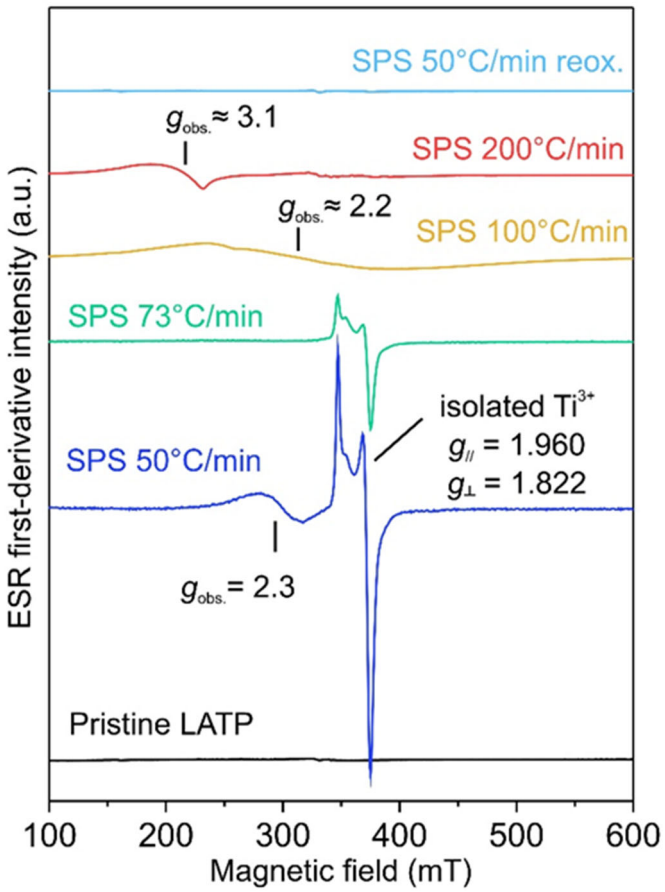

Figure 4: Low temperature (30 K) X-band ESR powder spectra obtained for pristine LATP, sintered samples (50°C/min, 73°C/min, 100°C/min and 200°C/min) and re-oxidized sample (reox.). All the spectra are normalised according to sample mass and all the spectroscopic parameters that can influence the ESR first-derivative curve intensity.

In order to characterize further the reactive processes involved during SPS sintering, ^{7}Li, ^{27}Al and ^{31}P solid state MAS NMR were performed. The series of ^{27}Al MAS NMR spectra recorded for the pristine LATP powder, the (conventional or by SPS) sintered and re-oxidized samples show two main signals around 38 ppm and -15 ppm (**Figure 5**), corresponding to AlO_4 (tetrahedral site) and AlO_6 (octahedral site) environments respectively. Deconvolution of the

spectra revealed, a single environment AlO_4 associated to the main impurity $AlPO_4$ already identified by XRD, and two AlO_6 environments at -15 ppm and -17.5 ppm. These resonances are characteristics for different local environments for aluminium in the NASICON phase[47–49]. The faster the heating rate used by SPS, the smaller the intensity of the signal associated to $AlPO_4$.This result is in good agreement with the observation made by XRD where the $AlPO_4$ impurity content in the pristine compound decreases during sintering as a result of the homogenization of the sample. Deconvolution of the different signals is given in **Table S2** and their quantification reveals that the ratio between AlO_4 and AlO_6 environments vary from 0.82 for the pristine, to 0.17 for the SPS 50°C/min sample and to 0.08 for SPS 200°C/min sample. In the pristine LATP, it corresponds to 45 mol.% of the total amount of Al in $AlPO_4$, and thus to an estimation of 0.14 mol. $AlPO_4$ for 1 mol. of LATP of composition $Li_{1.18}Al_{0.18}Ti_{1.82}(PO_4)_3$ (see more explanation in **Table S2** in supplementary information). For the SPS 50°C/min sample it leads to 0.04 mol. $AlPO_4$ for 1 mol. of LATP of composition $Li_{1.26}Al_{0.26}Ti_{1.74}(PO_4)_3$ and finally for the SPS 200°C/min sample to 0.02 mol. $AlPO_4$ for 1 mol. of LATP of composition $Li_{1.28}Al_{0.28}Ti_{1.72}(PO_4)_3$. These results are in good agreement with the XRD analyses, which show a decreasing amount of $AlPO_4$ impurity and lattice parameters for the NASICON phase in agreement with its enrichment in Al. Incorporation of more Al in the structure thanks to sintering, at equivalent composition for the overall sample, could also lead to the formation of a Ti-rich secondary phase that would be associated with the Ti^{3+} aggregates highlighted by ESR. This NMR quantification supported by ICP-OES and XRD analyses allows getting an in-depth knowledge of that complex electrolyte of general formulae LATP, whose chemistry is highly sensitive to synthesis and sintering conditions. It is also interesting to highlight that the sample SPS 50°C/min re-oxidized shows a very similar spectrum to that of pristine SPS 50°C/min, in good agreement with the small amount of Ti^{3+} estimated by ESR around 2.2 mol.% in the sample.

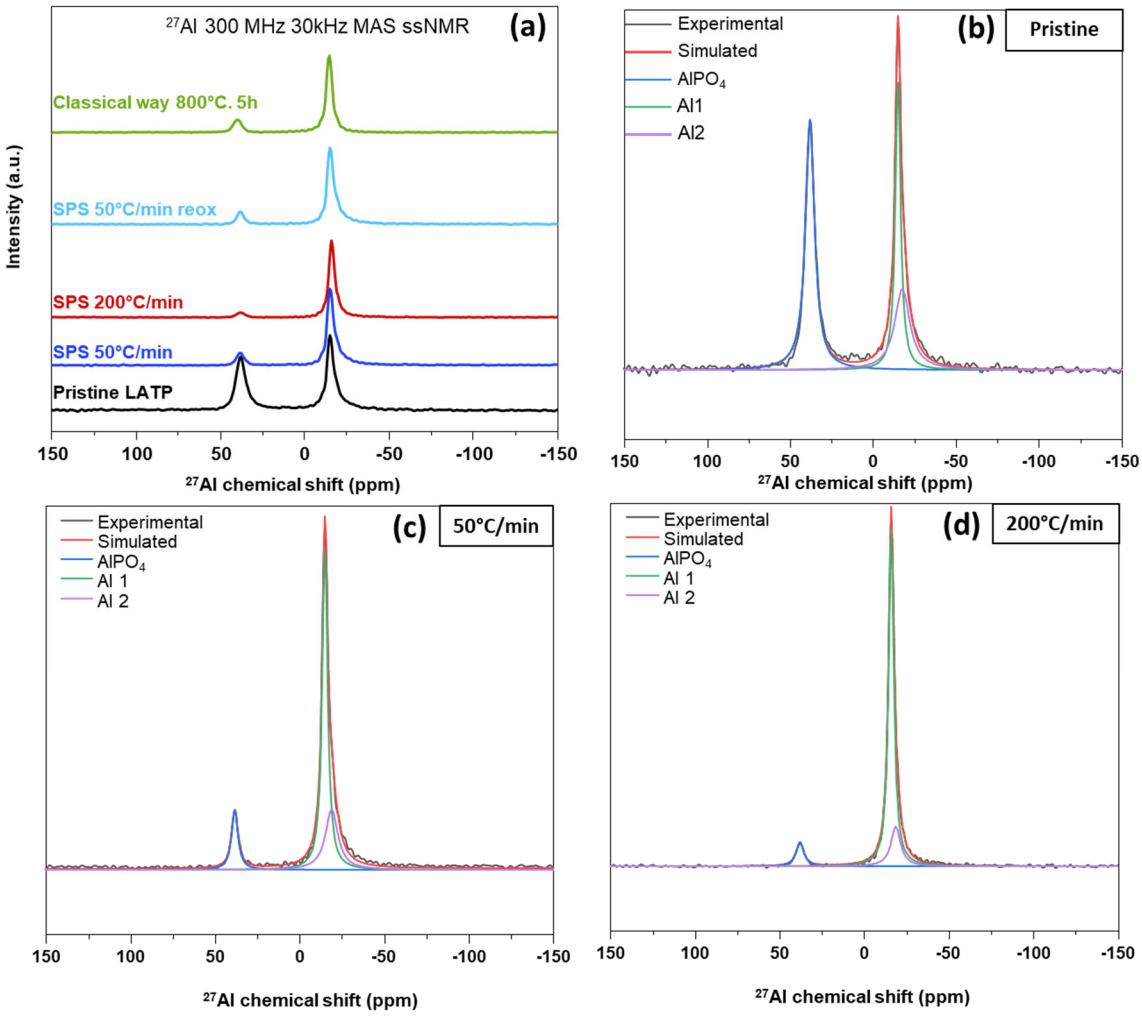

Figure 5: ^{27}Al NMR spectra of the pristine powder LATP, samples sintered by SPS and conventional annealing, and re-oxidized sample (a) and the deconvolution of the spectra collected for pristine LATP (b), SPS 50°C/min (c) and SPS 200°/min (d). The experimental and simulated spectra are displayed as black and red lines respectively. The simulated spectra are the sum of distinct line shapes displayed in blue, green and purple lines.

Figure 6 compares the ^{31}P MAS NMR spectra of the pristine LATP and samples sintered by SPS (SPS 50°C/min (before and after re-oxidation) and SPS 200°C/min) and by conventional process. An asymmetric resonance is observed between -23 and -27 ppm resulting from the superposition of several ^{31}P signals. Indeed, in $Li_{1+x}Al_xTi_{2-x}(PO_4)_3$, depending on the composition in Al, one can expect different ^{31}P environments versus Ti/Al that can be denoted as $P(OTi)_{4-n}(OAl)_n$ with n = 0, 1, 2, 3 or 4. This complexity would require for the fitting of the spectra to consider multiple environments and to constrain them to limit the number of

parameters (isotropic displacements, width and intensity of lines), as it was done by Arbi et al. for a series of high temperature crystalline phases of compositions $Li_{1+x}Al_xTi_{2-x}(PO_4)_3$.[47] The deconvolution of the ^{31}P MAS NMR spectrum collected for the LATP sample sintered by conventional annealing is given as an example in supplementary information in **Figure S5**. Here, only P environments with n = 0-3 are observed. A composition close to x = 0.1 is expected according to Arbi et al., and the NMR signal at -29 ppm supports also the presence of $AlPO_4$. Nevertheless, as also observed by Arbi et al.[47], despite the constraints imposed, in particular on the width of the different lines identified in a given spectrum, it is indeed surprising to observe that the width and isotropic displacement of the NMR signals vary widely from one sample to another for the same local environment. It makes thus difficult to compare quantitatively the results of these fittings. Nevertheless, as shown by the superposition of all the spectra given in **Figure 6b** the shape of the overall envelope obtained for the NMR signal gives interesting qualitative information about the composition of the NASICON phase and its evolution. This comparison allows highlighting a general peak broadening towards the more positive values and a “second contribution” centred at -26 ppm. This phenomenon is directly related to an evolution of the local environment of the P atoms with an enrichment of the sintered phases in Al. The faster the heating rate, the more enriched is the sintered material. Deconvolution of spectra is not presented here even if it has been attempted.

The NMR results obtained for the ^{27}Al and ^{31}P nuclei are perfectly consistent with the homogenisation of the material after sintering and, under certain conditions, with the quasi disappearance of the impurity $AlPO_4$ initially present, and therefore with enrichment of the NASICON structure in Al when the temperature rise is done quickly by SPS. Various environments of the ^{27}Al and ^{31}P nuclei could thus be highlighted by NMR.

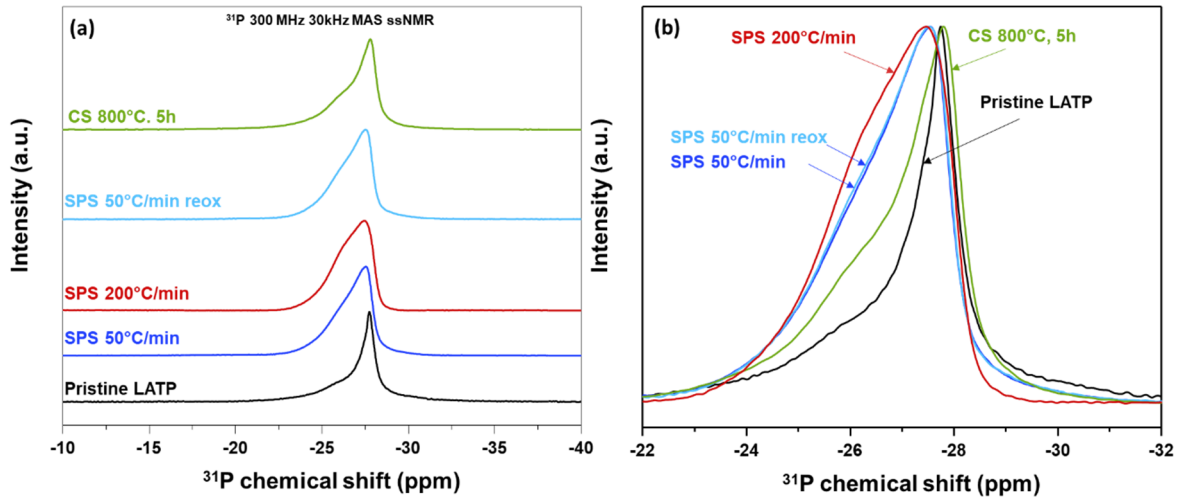

Figure 6: ^{31}P NMR spectra of the pristine powder LATP, sintered samples by SPS and conventional method, and re-oxidized sample (a) and the superposition of these spectra to highlight the local environment evolution (b). **Figure S5** gives as an example in supplementary information the deconvolution of the spectrum recorded for the sintered sample CS 800°C 5h.

Finally, ^{7}Li MAS NMR spectra given in **Figure 7** exhibit for each sample one single signal at -1.0 ppm except for the 200°C/min sample, which exhibits a signal around -1.2 ppm. The mobility of lithium ions within the NASICON phase depends on the sintering conditions used, in connection with the modification of its composition. The signals were fitted and corresponding parameters are given in **Table S3**. Two major contributions are observed at -1.04 and -0.62 ppm for the pristine powder. The first evolves to -1.02 and -1.25 ppm and the second to - 0.94 and - 1.18 ppm, for the two sintered samples SPS 50°C/min and SPS 200°C/min respectively. The relative intensity between the two contributions varies from 75:25 for the pristine sample, to 55:45 for the sample SPS 50°C/min and to 49:51 for the sample SPS 200°C/min. These evolutions reveal a modification of the Ti/Al environment around Li and of the Li distribution between the two Li sites, and in fact an enrichment of the NASICON structure in Al. Indeed, partial substitution of Ti^{4+} by Al^{3+} in the NASICON $LiTi_2(PO_4)_3$ structure induces an increase in the Li/metal ratio to compensate for the replacement of a Ti^{4+} ion in $LiTi_2(PO_4)_3$ with an Al^{3+} ion in $Li_{1+x}Al_xTi_{2-x}(PO_4)_3$ ($1Ti^{4+}$ is compensated by $1Al^{3+}$+$1Li^{+}$). Lithium

ions occupy two separate sites, the main site Li1 and the second site Li3, which is much more occupied as aluminium partially substitutes for titanium. The lithium ions diffuse within the LATP structure in zigzag from the $Li1O_6$ sites to the $Li3O_6$ sites, following the diffusion path Li1-Li3-Li3-Li1-Li3 etc. which shows the lowest activation energy. This distribution of lithium ions at the Li1 and Li3 sites in the mixed Al-Ti phase induces a decrease in the Li-Li distance, an increase in electrostatic repulsion between the Li^+ ions occupying the Li1 and Li3 sites and thus an increase in the ionic conductivity within the structure. The ^{7}Li NMR study shows that the faster the rise in temperature during SPS sintering, the sharper the signals obtained are, in good agreement with an increase in ion mobility and therefore Al content in the NASICON phase for these materials [47–50].

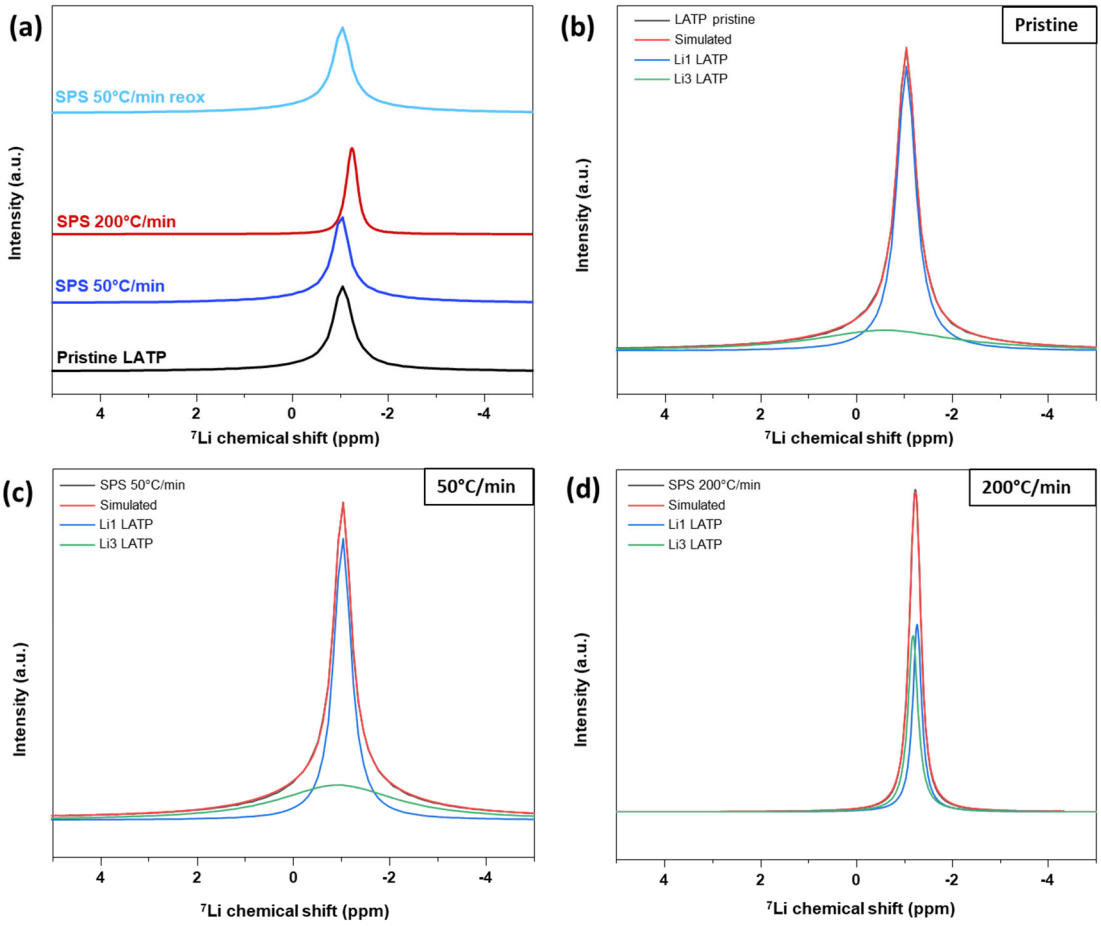

Figure 7: ^{7}Li NMR spectra of the pristine powder LATP, samples sintered by SPS at 50°C/min, before and after re-oxidation, and at 200°C/min (a). Deconvolution of each spectrum: pristine (b), SPS 50°C/min (c) and SPS 200°/min (d). The experimental and simulated spectra are displayed as black and red lines

respectively. The simulated spectrum is the sum of distinct line shapes displayed as blue and green lines.

Thus, the NMR studies demonstrate an homogenisation of the LATP structure during the SPS sintering process especially at fast heating rate in accordance with XRD data. Indeed, the ^{27}Al, ^{31}P and ^{7}Li MAS NMR, show clearly an Al phase enrichment during SPS at fast heating rate (as supported also by the evolution of the Raman spectra given in **Figure S6**[51–54]).

To understand in-depth surface modifications induced by the sintering process, XPS experiments were performed in order to compare the pristine and sintered samples. All of them were compared as powders, i.e. the sintered pellets were ground before the experiments in order to have access not only to the external surface of the pellets, but also to grain-boundary surface. XPS probing 3 to 10 nm in depth, composition at the extreme surface was compared to that of the bulk. Considering Ti $2p_{3/2}$ fitting, no obvious identification of Ti^{3+} could be done (no detection of a signal at 457.6 eV) for the blue colored SPS 50°C/min sample, as expected with only 2 mol.% at most as determined by ESR (below the resolution of the XPS technique). The most interesting information is the comparison of the XPS atomic ratios and their evolution depending on the sintering conditions. **Table 2** gathers the ratios Li/P, Al/P, Ti/P, Al/Ti and Li/Al at the SPS sample extreme surface and compares them to the pristine ones and the theoretical ones expected for $Li_{1.3}Al_{0.3}Ti_{1.7}(PO_4)_3$. First, the ratio Al/Ti determined at the surface of the pristine LATP powder is 0.67, much higher than the expected value of 0.18. Considering that we have shown that the pristine sample is a mixture between $AlPO_4$ and Al-poor LATP with 45% of Al contained in the former, this ratio of 0.67 is probably representative of a mixture of particles from one phase and from the other. For samples sintered by SPS, the increase of the heating rate causes first the decrease of Al/Ti ratio decrease at the surface, comparatively to that of the pristine sample (from 0.67 down to 0.34 for the sample SPS 25°C/min), before a considerable increase to reach 1 for the sample SPS 200°C°C/min. Therefore, there is clearly an overall Al-enrichment in the grain-boundary surface when the heating rate increases. At

first sight, this result seems conflicting with the other evidences of homogenization with an Al-enrichment of the LATP NASICON phase within the sintered pellets, which should lead to the convergence of sample's Al/Ti ratio towards the nominal value of 0.18 (see **Table 2**). However, this apparent disagreement falls down considering the complementary insight brought by surface techniques like XPS that probes only few nanometers in depth. Departing from a mixture of $AlPO_4$ and Al-poor LATP NASICON phase in the pristine powder, the evolution of Al/Ti or Al/P ratio revealed by XPS is in accordance with the homogenization of the samples sintered under slower heating rates (SPS 25°C/min, SPS 50°C/min and SPS 100°C/min). On the other hand, for samples sintered under faster heating rates such as the sample SPS 200°C/min, Al/Ti and Al/P ratios are even more discrepant than that of the pristine powder (see **Table 2**). Since this sample is one of the most homogeneous as probed by bulk techniques (XRD, NMR etc.), the most likely scenario is that the residual $AlPO_4$ is well spread at the grain-boundary of Al-enriched LATP phase. This general scheme allows to explain the enrichment of the NASICON phase in Al as identified by all the bulk characterization tools, from the long range to the local scales, and also, together the enrichment in Al of the 3 to 10 nm thick top layer probed by XPS, despite in proportion less Al remains as $AlPO_4$. The much smaller amount of $AlPO_4$ present in the sintered samples would form a thin film layer involving the grains, and thus much more detected by a surface technique.

It is important to mention that another hypothesis could have been the enhancement of x in $Li_{1+x}Al_xTi_{2-x}(PO_4)_3$ at the surface of the particles with the formation of a core-shell, the core and the shell being LATP NASICON phase, but the latter richer in Al than the first. Indeed, it is well known that the conductivity of LATP reaches an optimum for x equal to 0.3[40]. If x was bigger than 0.3 at the extreme surface, we could thus expect a drop in the conductivity because of less conductive grain boundaries. This hypothesis would be also in good agreement with the smaller quantity of $AlPO_4$ detected by XRD and NMR. Nevertheless, all together, other complementary considerations based on XRD and XPS tend to support the first hypothesis, *i.e.* the presence of a thin layer of $AlPO_4$ at the surface versus that of an enriched LATP with x

> 0.3. Thinner line shape is observed by XRD after sintering by SPS whereas a broadening could be expected for a gradient of compositions in the LATP particles. Nevertheless, for the second hypothesis we would expect a Li/Al ratio at the surface higher than 4.3 (for x > 0.3) as in the case of SPS 25°C/min sample. However, for the sample SPS 200°C/min it is observed an even smaller than 4.3 Li/Al ratio (**Table 2**), which is compatible with the hypothesis of a $AlPO_4$ thin film at the grain boundaries.

Table 2: Atomic ratios at the surface as obtained by XPS analyses. The theoretical values expected for $Li_{1.3}Al_{0.3}Ti_{1.7}(PO_4)_3$ are directly compared to those obtained for the pristine LATP powder and for the samples sintered from 25°C/min to 200°C/min as well as sample SPS 50°C/min reox.

	Surface				
Sample	***Li/P***	***Al/P***	***Ti/P***	***Al/Ti***	***Li/Al***
Nominal bulk	**0.43**	**0.1**	**0.57**	**0.18**	**4.3**
Pristine LATP	0.39	0.16	0.24	0.67	2.38
SPS 25°C/min	0.54	0.09	0.28	0.34	5.82
SPS 50°C/min	0.49	0.12	0.26	0.45	4.14
SPS 50°C/min reox	0.60	0.12	0.26	0.45	5.19
SPS 100°C/min	0.51	0.13	0.20	0.64	3.90
SPS 200°C/min	0.59	0.18	0.17	1.05	3.36

3.3 Impedance spectroscopy study

In the case of solid-state electrolytes, it is important to compare the transport properties of these samples sintered either by SPS or by conventional method. The total conductivity of the sintered samples was estimated from impedance spectroscopy measurements. **Figure 8** shows the Nyquist plot, -Z'' versus Z', of the sintered samples for the measurements performed at 25°C. The complex impedance data have been normalised regarding the shape factor (A/ l (surface/thickness)) of each sample as pellet. This normalisation allows a straight comparison of the impedance of the samples. Three contributions can be distinguished from the impedance

response of the sintered pellets: (i) a straight line in the low-frequency range (high Z') ascribed to polarization of the electrode due to lithium ions blocked by the metallic Au electrode, (ii) a big semi-circle in the medium-frequency range corresponding to grain boundary resistance, and (iii) a part of a small semi-circle in the high-frequency range pertaining to grain resistance. The polarization phenomenon in low-frequency range is a clear indication that ionic conductivity prevails over the electronic contribution, as expected for phosphates with NASICON-type structure. Since this structure is built of lantern units, with only corner-sharing between two octahedra and three phosphate groups, no electron hopping is possible between one transition metal and another. Regarding the high-frequency impedance response associated to the grain contribution, the observation of this semi-circle is compromised due to the frequency range limitations of the measurement and the intrinsic high grain conductivity of the LATP ceramics. In this case, only the total conductivity (σ) was determined from the resistance (σ=l/RA) which is itself determined employing a suitable equivalent circuit to fit the impedance spectra **(Figure 8)**. It should be noted that for the sample SPS 300°C/min an additional R|CPE needs to be added in series to grain and grain boundary contributions to properly fit the impedance data. As it has already been extensively discussed in the literature, the total conductivity of ion-conducting ceramic electrolytes is mostly limited by the grain boundaries resistance. For instance, the typical grain ionic conductivity of LATP is in the order

of 10^{-3} $\Omega^{-1}.cm^{-1}$, which is at least one order of magnitude higher than the typical grain-boundary conductivity in this material.[55]

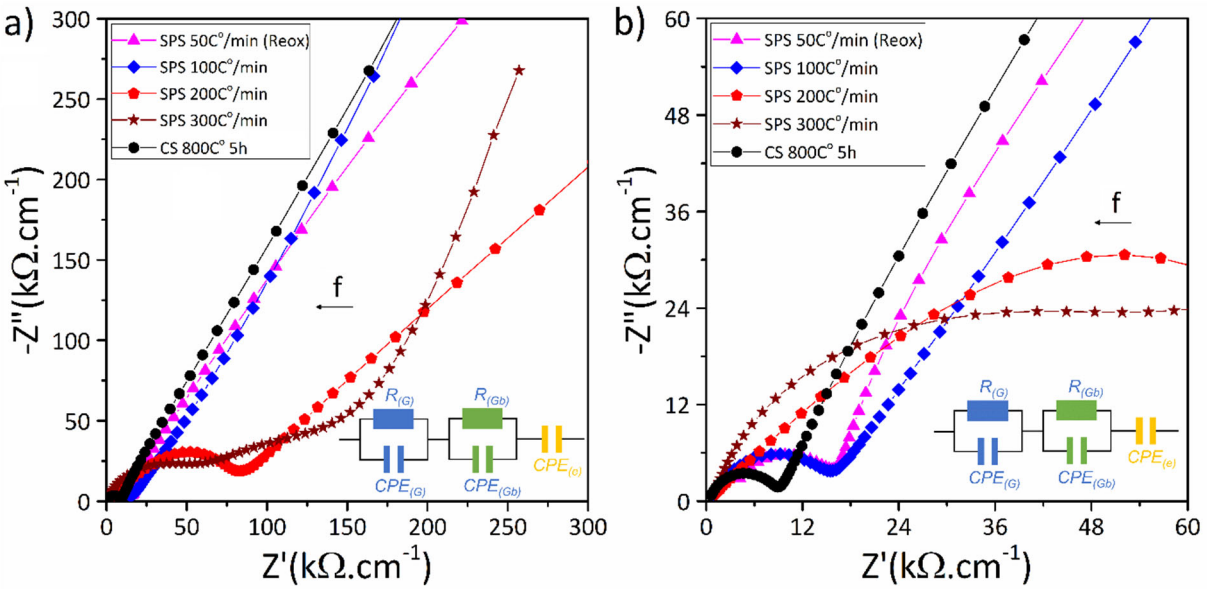

Figure 8: Impedance data recorded at 25°C for LATP samples sintered, either 5 min by SPS at heating rates of 50°C/min after reoxidation, 100°C/min and 200°C/min, or by conventional method at 800°C (5h) (a). Enlargements are given from 0 to 60 kΩ.cm to better observe changes at high frequencies for the different samples (b). The complex impedance data shown here have been normalized regarding the shape factor of each sample for comparison purposes. The equivalent circuit used to fit the impedance data including a parallel combination of a resistance (R_G) and a constant-phase element (CPE_G) attributed to the grain contribution, in series with a parallel combination of a resistance (R_{GB}) and a constant-phase element (CPE_{GB}) attributed to the grain boundary contribution, and a constant-phase element (CPE_e) that accounts for the electrode polarization effects in the low frequency region.

Concerning the overall conductivity of SPS sintered samples, the faster the heating rate the higher is the medium frequency semi-circle and consequently the lower is the total conductivity (**Table 3**). These results seem to be in contradiction with those reported in literature, which most often report an enhancement of overall conductivity with the increase of crystalline domain or grain size. Furthermore, since in this case the enrichment in aluminium of the NASICON phase is observed, this major phase could also contribute to an increase in the overall ionic conductivity [60]. However, this increase in conductivity would be in that case restricted to the grain contribution which is not the limiting contribution in NASICON-type LATP.

Indeed, our results indicate that it is the chemical nature of the grain boundaries that control the ionic conductivity of these sintered submicronic LATP samples [42,56–58]. The fact that the sample SPS 300°C/min is much more resistive than the others and shows a third semi-circle in middle-frequency range, is by itself an indication of the presence of an insulating phase in the grain boundaries. The best ionic conductivity obtained for samples sintered by SPS at 750°C is 7.1 x 10^{-5} $\Omega^{-1}.cm^{-1}$ for the SPS 50°C/min sample. Note furthermore that the overall conductivity does not seem to be impacted by the presence of a very small amount of Ti^{3+} ions in the material (**Figure S7**) since similar conductivity is found after re-oxidation of the sample under oxygen (conductivity of 6.9 x 10^{-5} Ω^{-1} cm^{-1}, see **Table 3**). This latter comparison highlights further that the electronic contribution to the overall conductivity should be negligible even in the case of the SPS 50°C/min sample containing Ti^{3+}.

Table 3: Ionic conductivity obtained at room temperature for LATP samples sintered either 5 min by SPS at heating rates of 50°C/min (before and after reoxidation), 100°C/min and 200°C/min or by conventional method at 800°C (5h) as well as their respective activation energies.

Sample	σ_{298K} (Ω^{-1} cm^{-1})	E_a
SPS 50°C/min (Reox)	6.9E-5	0.382(3)
SPS 50°C/min	7.1E-5	-
SPS 100°C/min	6.6E-5	0.369(3)
SPS 200°C/min	1.3E-5	0.52(1)
SPS 300°C/min	6.4E-6	-
CS 800°C 5h	1.2E-4	0.404(4)

The dependence of the overall electrical conductivity as a function of the inverse of temperature is investigated employing the Arrhenius law: $\sigma = \frac{\sigma_0}{T} e^{\frac{-E_a}{kT}}$ with σ, the ionic conductivity of the solid electrolyte, σ_0 a pre-exponential term, E_a the activation energy, k the Boltzmann constant and T the temperature. Thus, the activation energy for the ionic conductivity can be estimated from the slope of linear fit[59]. This methodology has been applied for different samples: SPS 50°C/min after reoxidation, SPS 100°C/min, SPS 200°C/min and

that sintered by conventional method. **Figure 9** shows the dependence of the overall electrical conductivity as a function of the inverse of temperature for those samples and their corresponding activation energy. The results indicate that the increase of the heating rate tends to increase the activation energy, changing from 0.382 ± 0.003 eV for the SPS 50°C/min re-oxidized sample to 0.52 ± 0.01 eV for the SPS 200°C/min sample. These results confirm the observations made regarding the ionic conductivity, the faster the temperature rise ramp, the more resistive the grain boundaries become, reducing the ionic conductivity of the material. This decrease of the conductivity could be explained by the enrichment of Al in the grain boundaries identified by XPS forming a resistive layer, despite the bulk LATP shows an overall composition expected to be the more conductive. $AlPO_4$ is known to present much lower ionic conductivity than LATP with a NASICON-like structure. Besides, the overall conductivity of the dual-phase ceramic pellet will depend not only on the relative amount of these two phases but also how this secondary phase is distributed in the grain boundaries. For instance, if the $AlPO_4$ phase is mainly located as inclusions in the corners of grain boundaries, the impact in the overall conductivity of the pellet will be minimal. Conversely, if the $AlPO_4$ phase is well dispersed enveloping the LATP grains the detrimental impact of this phase on overall conductivity will be maximized. In our case, we hypothesize that, even though the $AlPO_4$ content decreases in the samples sintered at high heating rate, the $AlPO_4$ is better spread in the grain boundaries on these samples. Another possible hypothesis is that the $AlPO_4$ is incorporated in the surface of the LATP grains causing a stoichiometric shift on the LATP phase which results in a drop in the overall conductivity.

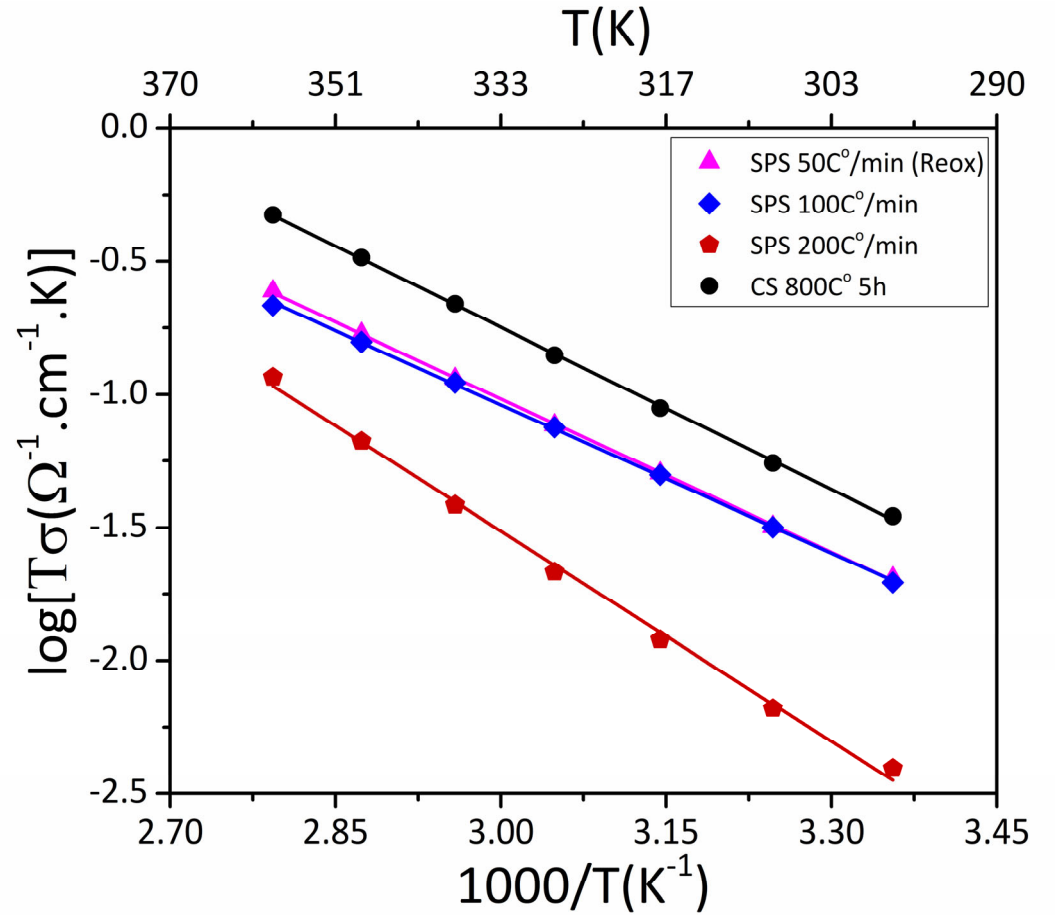

Figure 9: Arrhenius plot for estimation of the activation energy of samples sintered by SPS at heating rates of 50°C/min to 200°C/min compared to that of the one sintered by conventional method.

4. Conclusion

This work is dedicated to the study of the reactivity of submicronic LATP particles during sintering by SPS, this morphology being of interest for LATP to be used in conductive electrolytic membrane or in catholyte (mixed with the positive electrode material) in inorganic all-solid-state batteries. The particles size as well as the actual purity and composition of the solid electrolyte NASICON-type powder are critical. We have shown that the impurity $AlPO_4$, commonly observed in NASICON LATP, plays a major role on the conductivity depending on its content and distribution within the composite. Sintering by SPS allows to reach, at lower temperature and in few minutes instead of few hours, higher densification than conventional method (95 % *vs.* 90 %), but the conditions used have major impacts on the crystallinity,

microstructure, composition and thus conductivity of the composite containing LATP as major phase. These SPS sintering parameters have thus to be explored and optimized in each case, depending on the chemistry and properties targeted. For the submicronic LATP powder as studied, despite inducing partial reduction of Ti^{4+} into Ti^{3+} and a colour change of the pellet from white to blue, slow heating rate (50°C/min) with a sintering temperature of 750°C allows reaching similar conductivity but higher densification of 95% than the conventional sintering. On the contrary, despite no reduction of Ti, an enrichment in Al of the LATP NASICON phase and a high densification of 95% that were expected to lead all together to a higher overall conductivity, fast heating rates by SPS caused degradation of the transport properties. The optimized composition obtained in these conditions for LATP (i.e. close to $Li_{1.3}Al_{0.3}Ti_{1.7}(PO_4)_3$) is in fact not sufficient, as counterbalanced by its covering by a resistive thin layer and thus an increasing grain boundaries resistance.

The understanding of these complex sintering processes and reactivity requires to combine multiscale advanced characterizations (here XRD, NMR, ESR and XPS), from the long range to the local scales and from the bulk to the surface of the particles. Only this powerful scrutinization allows understanding why the apparently optimized (purest and most densified) material shows unexpected properties.

ASSOCIATED CONTENT

Supporting information

The Supplementary Information contains scanning electron microscopy images of the pristine LATP and its chemical analysis, full angular range XRD patterns of the series of samples reported in the paper and the corresponding lattice parameters, Rietveld refinements of the XRD patterns collected for four samples, the low-temperature X band ESR spectrum for one sample, the NMR parameters determined from the fit of the spectra of few samples, as well as the Raman spectra for few samples.

AUTHOR INFORMATION

Corresponding Authors

Laurence Croguennec: Laurence.croguennec@icmcb.cnrs.fr

Rafaël Bianchini-Nuernberg: rafael.bianchini-nuernberg@icmcb.cnrs.fr

ACKNOWLEDGEMENTS

The authors acknowledge ANRT, Renault SAS and Région Nouvelle-Aquitaine for the funding of the project, ANRT and Renault SAS for the funding (CIFRE grant) of G. C.'s PhD thesis, Alistore-ERI for the funding of J. S. S.'s postdoctoral fellowship, as well as the French National Research Agency (STORE-EX Labex Project ANR-10-LABX-76-01) for financial support for their research on the electrochemical energy storage. The authors thank Emmanuel Petit and François Weill at ICMCB for scientific discussions. The authors also thank Cathy Denage, Jérôme Kalisky and Eric Lebraud at ICMCB for their technical support for ICP-OES, SEM and XRD respectively, as well as Philippe Legros, Mélanie Vaudescal and Nithavong Cam at PLACAMAT for their scientific support with SEM and Nano Auger analyses.

REFERENCES

1. Tarascon, J.-M. & Armand, M. Issues and challenges facing rechargeable lithium batteries. in *Materials for Sustainable Energy* 171–179 (Co-Published with Macmillan Publishers Ltd, UK, 2010).
2. Noh, H.-J., Youn, S., Yoon, C. S. & Sun, Y.-K. Comparison of the structural and electrochemical properties of layered Li[NixCoyMnz]O2 (x = 1/3, 0.5, 0.6, 0.7, 0.8 and 0.85) cathode material for lithium-ion batteries. *J. Power Sources* **233**, 121–130 (2013).
3. Chen, C. H. *et al.* Aluminum-doped lithium nickel cobalt oxide electrodes for high-power lithium-ion batteries. *J. Power Sources* **128**, 278–285 (2004).
4. Wild, M. *et al.* Lithium sulfur batteries, a mechanistic review. *Energy Environ. Sci.* **8**, 3477–3494 (2015).

5. Geng, D. *et al.* From Lithium-Oxygen to Lithium-Air Batteries: Challenges and Opportunities. *Adv. Energy Mater.* **6**, 1502164 (2016).
6. Zhang, C. *et al.* Progress and prospects of next-generation redox flow batteries. *Energy Storage Mater.* **15**, 324–350 (2018).
7. Zaman, W. & Hatzell, K. B. Processing and manufacturing of next generation lithium-based all solid-state batteries. *Curr. Opin. Solid State Mater. Sci.* **26**, 101003 (2022).
8. Kim, J. G. *et al.* A review of lithium and non-lithium based solid state batteries. *J. Power Sources* **282**, 299–322 (2015).
9. Lou, S. *et al.* Interface Issues and Challenges in All-Solid-State Batteries: Lithium, Sodium, and Beyond. *Adv. Mater.* **33**, 2000721 (2021).
10. Nowak, S. & Winter, M. Review—Chemical Analysis for a Better Understanding of Aging and Degradation Mechanisms of Non-Aqueous Electrolytes for Lithium Ion Batteries: Method Development, Application and Lessons Learned. *J. Electrochem. Soc.* **162**, A2500–A2508 (2015).
11. Lu, Y., Li, L., Zhang, Q., Niu, Z. & Chen, J. Electrolyte and Interface Engineering for Solid-State Sodium Batteries. *Joule* **2**, 1747–1770 (2018).
12. Manthiram, A., Yu, X. & Wang, S. Lithium battery chemistries enabled by solid-state electrolytes. *Nat. Rev. Mater.* **2**, 16103 (2017).
13. Bucharsky, E. C., Schell, K. G., Hintennach, A. & Hoffmann, M. J. Preparation and characterization of sol–gel derived high lithium ion conductive NZP-type ceramics Li1+x AlxTi2−x(PO4)3. *Solid State Ion.* **274**, 77–82 (2015).
14. DeWees, R. & Wang, H. Synthesis and Properties of NaSICON-type LATP and LAGP Solid Electrolytes. *ChemSusChem* **12**, 3713–3725 (2019).
15. Aatiq, A., Ménétrier, M., Croguennec, L., Suard, E. & Delmas, C. On the structure of $Li_3Ti_2(PO_4)_3$. *J Mater Chem* **12**, 2971–2978 (2002).
16. Pfalzgraf, D., Mutter, D. & Urban, D. F. Atomistic analysis of Li migration in Li1+AlTi2−(PO4)3 (LATP) solid electrolytes. *Solid State Ion.* **359**, 115521 (2021).

17. Xiao, W., Wang, J., Fan, L., Zhang, J. & Li, X. Recent advances in Li1+xAlxTi2−x(PO4)3 solid-state electrolyte for safe lithium batteries. *Energy Storage Mater.* **19**, 379–400 (2019).
18. Aono, H., Sugimoto, E., Sadaoka, Y., Imanaka, N. & Adachi, G. Ionic Conductivity of Solid Electrolytes Based on Lithium Titanium Phosphate. *J. Electrochem. Soc.* **137**, 1023–1027 (1990).
19. Waetzig, K. *et al.* Synthesis and sintering of Li1.3Al0.3Ti1.7(PO4)3 (LATP) electrolyte for ceramics with improved Li+ conductivity. *J. Alloys Compd.* **818**, 153237 (2020).
20. Xu, X., Wen, Z., Yang, X. & Chen, L. Dense nanostructured solid electrolyte with high Li-ion conductivity by spark plasma sintering technique. *Mater. Res. Bull.* **43**, 2334–2341 (2008).
21. Rosenberger, A., Gao, Y. & Stanciu, L. Field-assisted sintering of Li1.3Al0.3Ti1.7(PO4)3 solid-state electrolyte. *Solid State Ion.* **278**, 217–221 (2015).
22. Wang, C. *et al.* A general method to synthesize and sinter bulk ceramics in seconds. *Science* **368**, 521–526 (2020).
23. Hallopeau, L. *et al.* Microwave-assisted reactive sintering and lithium ion conductivity of Li1.3Al0.3Ti1.7(PO4)3 solid electrolyte. *J. Power Sources* **378**, 48–52 (2018).
24. Gao, L., Hong, J. S., Miyamoto, H. & Torre, S. D. D. L. Bending strength and microstructure of Al2O3 ceramics densified by spark plasma sintering. *J. Eur. Ceram. Soc.* **20**, 2149–2152 (2000).
25. Wang, S. W., Chen, L. D. & Hirai, T. Densification of Al $_2$ O $_3$ Powder Using Spark Plasma Sintering. *J. Mater. Res.* **15**, 982–987 (2000).
26. Takeuchi, T., Tabuchi, M., Kageyama, H. & Suyama, Y. Preparation of Dense BaTiO3 Ceramics with Submicrometer Grains by Spark Plasma Sintering. *J. Am. Ceram. Soc.* **82**, 939–943 (1999).
27. Li, W. & Gao, L. Rapid sintering of nanocrystalline ZrO2(3Y) by spark plasma sintering. *J. Eur. Ceram. Soc.* **20**, 2441–2445 (2000).
28. Tokita, M. Progress of Spark Plasma Sintering (SPS) Method, Systems, Ceramics Applications and Industrialization. *Ceramics* **4**, 160–198 (2021).
29. Lachal, M. *et al.* Flash sintering of cationic conductive ceramics: A way to build multilayer systems. *J. Am. Ceram. Soc.* **104**, 3845–3854 (2021).

30. Delaizir, G., Manafi, N., Jouan, G., Rozier, P. & Dollé, M. All-solid-state silver batteries assembled by Spark Plasma Sintering. *Solid State Ion.* **207**, 57–63 (2012).
31. Delaizir, G. *et al.* The Stone Age Revisited: Building a Monolithic Inorganic Lithium-Ion Battery. *Adv. Funct. Mater.* **22**, 2140–2147 (2012).
32. Aboulaich, A. *et al.* A New Approach to Develop Safe All-Inorganic Monolithic Li-Ion Batteries. *Adv. Energy Mater.* **1**, 179–183 (2011).
33. Zhu, H. & Liu, J. Emerging applications of spark plasma sintering in all solid-state lithium-ion batteries and beyond. *J. Power Sources* **391**, 10–25 (2018).
34. Massiot, D. *et al.* Modelling one- and two-dimensional solid-state NMR spectra: Modelling 1D and 2D solid-state NMR spectra. *Magn. Reson. Chem.* **40**, 70–76 (2002).
35. Noh, J. H. *et al.* Enhancing the Densification of Nanocrystalline TiO_2 by Reduction in Spark Plasma Sintering. *J. Am. Ceram. Soc.* **93**, 993–997 (2010).
36. Cavaliere, P., Sadeghi, B. & Shabani, A. Spark Plasma Sintering: Process Fundamentals. in *Spark Plasma Sintering of Materials* (ed. Cavaliere, P.) 3–20 (Springer International Publishing, 2019).
37. Lee, G. *et al.* Effect of electric current on densification behavior of conductive ceramic powders consolidated by spark plasma sintering. *Acta Mater.* **144**, 524–533 (2018).
38. Shannon, R. D. & Prewitt, C. T. Effective ionic radii in oxides and fluorides. *Acta Crystallogr. B* **25**, 925–946 (1969).
39. Redhammer, G. J. *et al.* A single crystal X-ray and powder neutron diffraction study on NASICON-type Li1+Al Ti2−(PO4)3 (0 ≤ x ≤ 0.5) crystals: Implications on ionic conductivity. *Solid State Sci.* **60**, 99–107 (2016).
40. Bucharsky, E. C., Schell, K. G., Hintennach, A. & Hoffmann, M. J. Preparation and characterization of sol–gel derived high lithium ion conductive NZP-type ceramics Li1+x AlxTi2−x(PO4)3. *Solid State Ion.* **274**, 77–82 (2015).
41. Chang, C.-M., Lee, Y. I., Hong, S.-H. & Park, H.-M. Spark Plasma Sintering of LiTi2(PO4)3-Based Solid Electrolytes. *J. Am. Ceram. Soc.* **88**, 1803–1807 (2005).

42. Jackman, S. D. & Cutler, R. A. Effect of microcracking on ionic conductivity in LATP. *J. Power Sources* **218**, 65–72 (2012).

43. Yamaga, M., Yosida, T., Naitoh, Y. & Kodama, N. Electron paramagnetic resonance and optical spectroscopy of Ti-doped $CaYAlO_4$. *J. Phys. Condens. Matter* **6**, 4381–4394 (1994).

44. Maurelli, S., Vishnuvarthan, M., Berlier, G. & Chiesa, M. NH3 and O_2 interaction with tetrahedral Ti^{3+} ions isomorphously substituted in the framework of TiAlPO-5. A combined pulse EPR, pulse ENDOR, UV-Vis and FT-IR study. *Phys Chem Chem Phys* **14**, 987–995 (2012).

45. Abraham, M. M. & Bamberger, C. E. Electron Paramagnetic Resonance Spectroscopic Determination of Ti3+ in Several Titanium Phosphate Compounds. *J. Am. Ceram. Soc.* **74**, 2299–2300 (1991).

46. Ding, C.-C. *et al.* An investigation on the defect structures and spin Hamiltonian parameters for the two orthorhombic Ti3+ centers in ZnWO4. *J. Phys. Chem. Solids* **86**, 141–147 (2015).

47. Arbi, K., Mandal, S., Rojo, J. M. & Sanz, J. Dependence of Ionic Conductivity on Composition of Fast Ionic Conductors $Li_{1+x}Ti_{2-x}Al_x(PO_4)_3$, $0 \le x \le 0.7$. A Parallel NMR and Electric Impedance Study. *Chem. Mater.* **14**, 1091–1097 (2002).

48. Arbi, K., Bucheli, W., Jiménez, R. & Sanz, J. High lithium ion conducting solid electrolytes based on NASICON Li 1+x Al x M 2−x (PO 4) 3 materials (M = Ti, Ge and 0 ≤ x ≤ 0.5). *J. Eur. Ceram. Soc.* **35**, 1477–1484 (2015).

49. Kwatek, K., Ślubowska, W., Trébosc, J., Lafon, O. & Nowiński, J. L. Structural and electrical properties of ceramic Li-ion conductors based on Li1.3Al0.3Ti1.7(PO4)3-LiF. *J. Eur. Ceram. Soc.* **40**, 85–93 (2020).

50. Kahlaoui, R. *et al.* Cation Miscibility and Lithium Mobility in NASICON $Li_{1+x}Ti_{2-x}Sc_x(PO_4)_3$ ($0 \le x \le 0.5$) Series: A Combined NMR and Impedance Study. *Inorg. Chem.* **56**, 1216–1224 (2017).

51. Burba, C. & Frech, R. Vibrational spectroscopic study of lithium intercalation into LiTi2(PO4)3. *Solid State Ion.* **177**, 1489–1494 (2006).

52. Venkateswara Rao, A., Veeraiah, V., Prasada Rao, A. V., Kishore Babu, B. & Brahmayya, M. Spectroscopic characterization and conductivity of Sn-substituted LiTi2(PO4)3. *Res. Chem. Intermed.* **41**, 4327–4337 (2015).

53. Cretin, M., Fabry, P. & Abello, L. Study of Li1 + xAlxTi2 − x(PO4)3 for Li+ potentiometric sensors. *J. Eur. Ceram. Soc.* **15**, 1149–1156 (1995).

54. Giarola, M. *et al.* Structure and Vibrational Dynamics of NASICON-Type $LiTi_2(PO_4)_3$. *J. Phys. Chem. C* **121**, 3697–3706 (2017).

55. Pérez-Estébanez, M., Isasi-Marín, J., Többens, D. M., Rivera-Calzada, A. & León, C. A systematic study of Nasicon-type Li1+xMxTi2−x(PO4)3 (M: Cr, Al, Fe) by neutron diffraction and impedance spectroscopy. *Solid State Ion.* **266**, 1–8 (2014).

56. Hupfer, T. *et al.* Evolution of microstructure and its relation to ionic conductivity in Li1+xAlxTi2−x(PO4)3. *Solid State Ion.* **288**, 235–239 (2016).

57. Waetzig, K., Rost, A., Langklotz, U., Matthey, B. & Schilm, J. An explanation of the microcrack formation in Li 1.3 Al 0.3 Ti 1.7 (PO 4) 3 ceramics. *J. Eur. Ceram. Soc.* **36**, 1995–2001 (2016).

58. Nuernberg, R. B. & Rodrigues, A. C. M. A new NASICON lithium ion-conducting glass-ceramic of the Li1+xCrx(GeyTi1−y)2−x(PO4)3 system. *Solid State Ion.* **301**, 1–9 (2017).

59. Nuernberg, R. B. Numerical comparison of usual Arrhenius-type equations for modeling ionic transport in solids. *Ionics* **26**, 2405–2412 (2020).